ACS APPLIED MATERIALS & INTERFACES | Letter
Cite This: ACS Appl. Mater. Interfaces XXXX, XXX, XXX−XXX | www.acsami.org

High-Efficiency Monolayer Molybdenum Ditelluride Light-Emitting Diode and Photodetector

Yi Zhu,[†,‡] Ziyuan Li,[‡] Linglong Zhang,[†] Bowen Wang,[†] Zhenqing Luo,[†] Jianzheng Long,[†] Jiong Yang,[†] Lan Fu,[*,‡] and Yuerui Lu[*,†]

[†]Research School of Engineering, College of Engineering and Computer Science, and [‡]Department of Electronic Materials Engineering, Research School of Physics and Engineering, The Australian National University, Canberra, Australian Capital Territory 2601, Australia

Supporting Information

Downloaded via UNIV OF TEXAS AT EL PASO on November 6, 2018 at 01:03:41 (UTC).
See https://pubs.acs.org/sharingguidelines for options on how to legitimately share published articles.

ABSTRACT: Developing a high-efficiency and low-cost light source with emission wavelength transparent to silicon is an essential step toward silicon-based nanophotonic devices and micro/nano industry platforms. Here, a near-infrared monolayer $MoTe_2$ light-emitting diode (LED) has been demonstrated and its emission wavelength is transparent to silicon. By taking advantage of the quantum tunneling effect, the device has achieved a very high external quantum efficiency (EQE) of 9.5% at 83 K, which is the highest EQE obtained from LED devices fabricated from monolayer TMDs so far. When the device is operated as a photodetector, the $MoTe_2$ device exhibits a strong photoresponsivity at resonant wavelength 1145 nm. The low dark current of ∼5pA and fast response time 5.06 ms are achieved due to suppression of hBN tunneling layer. Our results open a new route for the investigation of novel near-infrared silicon integrated optoelectronic devices.

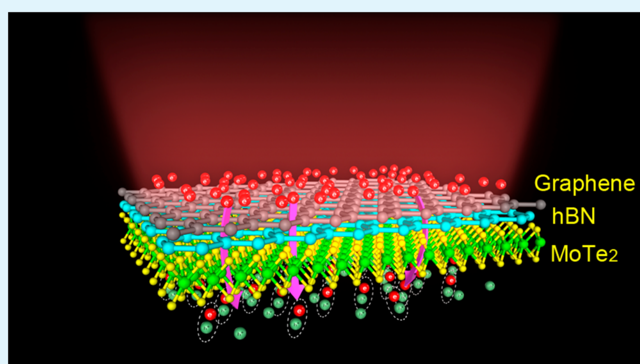

KEYWORDS: *molybdenum ditelluride, light emitting diode, quantum efficiency, tunneling effect, near-infrared*

1. INTRODUCTION

Recently, monolayer TMDs have attracted tremendous attention because of their unique properties, including the indirect-to-direct bandgap transition,[1,2] the large exciton and trion binding energy,[3,4] and tunable band alignment[5] in atomically thin layers. Those distinct properties make them promising active materials for next-generation optoelectronic applications, including excitonic lasers,[6] photodetectors,[7] and LEDs.[8] Currently, much effort has been put to investigate TMD-based LEDs in the visible range. Research progress in the near-infrared to infrared range has been barely reported. However, the infrared light source is usually a key component of on-chip silicon-based optical interconnects and high-speed communication systems. Thus, to explore and fabricate high-efficiency advanced infrared LED light sources becomes a crucial task. Typically, there are two popular architectures for fabricating TMD-based LED devices. One is lateral monolayer devices[9,10] by using electrostatic doping to form an adjacent p−n junction within the material. The other one is vertical tunneling devices[11−13] that artificially introduce quantum wells (QWs) to engineer the recombination of electrons and holes. EQE is considered to be a critical parameter in LED devices. By using splitting gates, Ross et al. have reported a lateral p−n junction monolayer WSe_2 LED with ∼1% efficiency.[10] They also demonstrated that emissions of LED can be tuned between excitons and trions via modulating the injection bias. Compared to the lateral structure, a vertical structure allows higher injection current efficiency via larger contact area, more emission area, and thus higher efficiency. Although a high EQE (∼8.4% at 6 K) has been achieved by using multiple QWs,[14] the quantum efficiency for most single QW TMD-based LED is still quite low. Withers et al. have demonstrated a vertical tunneling $MoSe_2$ LED and a tunneling WSe_2 LED by using boron nitride as tunnel barriers and graphene as contact electrodes.[13] They reported that the monolayer WSe_2 tunneling LED achieved 5% efficiency at room temperature. Besides, Carmen el at also successfully demonstrated the vertical tunneling WSe_2 and WS_2 quantum LED devices by taking advantage of boron nitride as tunnel layer.[12] They proposed that those LED devices have single photon behavior. In addition, the emission wavelength of lateral or vertical structure LED devices have been limited within CCD detection range so far and silicon (Si) or silicon dioxide (SiO_2) is used as host substrates. However, silicon substrate itself has a very strong absorption in CCD detection range. F. Withers et al.[13] reported that, in a monolayer tungsten

Received: August 15, 2018
Accepted: November 1, 2018
Published: November 1, 2018

© XXXX American Chemical Society

DOI: 10.1021/acsami.8b14076
ACS Appl. Mater. Interfaces XXXX, XXX, XXX−XXX

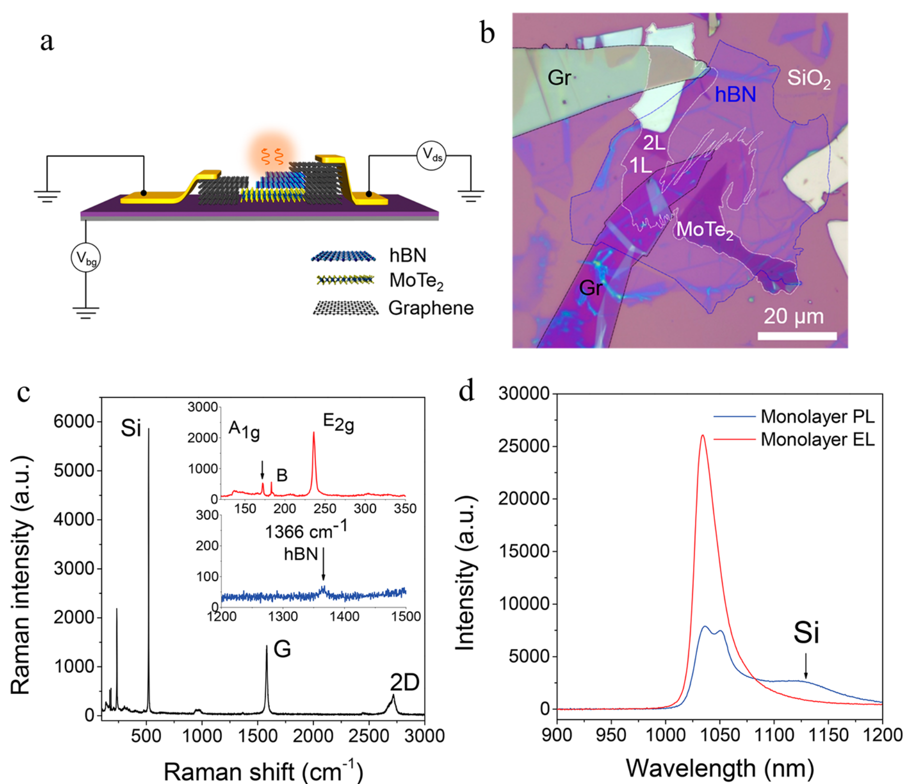

Figure 1. Architecture of monolayer $MoTe_2$ LED. (a) Schematic of our monolayer $MoTe_2$ LED and electrical connections for EL measurements. (b) Optical microscope image of the monolayer $MoTe_2$ LED. The white, blue, and black dashed line outline the footprint of $MoTe_2$, hBN, and graphite, respectively. Monolayer and bilayer $MoTe_2$ area are marked as 1L and 2L. (c) Raman spectrum of the $MoTe_2$/hBN/graphite overlapping area. Inset: Zoom-in Raman peak of the $MoTe_2$ (red curve) and the hBN (blue curve). (d), Measured PL and EL spectrum from the same location of the monolayer $MoTe_2$ LED device at 83 K. The injection current for EL emission is 6.07 μA under back gate voltage at −20 V.

diselenide (WSe_2) LED with highly reflective distributed Bragg reflector (DBR) substrates, the EQE reached 5% at room temperature. Up to 30% of the emitted light could be collected by the detector for LEDs based on such DBR substrate compared to only 2% from those with Si/SiO_2 substrates. To achieve a high-efficiency infrared light source, a high-quality optical gain material is necessary. Monolayer $MoTe_2$, a special family member of two-dimensional (2D) TMDs, has an electrical bandgap of ~1.72 eV.[4,15] The exciton emission peak from monolayer $MoTe_2$ is located at ~1.1 eV[15] and is very close to the silicon bandgap, making it nearly transparent for silicon, which is essential for on-chip integrated high-efficiency silicon photonics and optoelectronics. Bilayer $MoTe_2$ has been successfully demonstrated to fabricate infrared LEDs and photodetectors by applying electrostatic doping to form a lateral adjacent p−n junction.[16] However, this electrostatic doping method is more difficult to achieve in monolayer $MoTe_2$ because of the complicated fabrication process and low electrical excitation tolerance. In this work, we demonstrate the vertical structure monolayer $MoTe_2$ LED via a solution- and lithography-free transfer process. The total emission area reaches 80 μm^2. Importantly, we show that our $MoTe_2$ LED device has an extremely high EQE of around 9.5% at 83K, which is the highest EQE that has been achieved in monolayer TMD LEDs. Moreover, this vertical structure can also be extended to be a photodetector. The response time of our $MoTe_2$ photodetector has been measured to be ~5.06 ms with an extremely low dark current of ~5 pA, which is comparable to other $MoTe_2$-based photodetectors.[17] Our results pave the way for the investigation of the next-generation silicon-integrated on-chip infrared optoelectronic devices.

2. EXPERIMENTAL SECTION

2.1. Device Fabrication and Characterization. The Monolayer $MoTe_2$ and the few layers hBN were mechanically exfoliated onto the SiO_2/Si substrate. Transfer stacking process was done with a homemade transfer platform (Supporting Note 1). The 100 nm thickness gold electrodes were directly patterned in a plain SiO_2/Si substrate by conventional photolithography, metal deposition and lift-off process. The homemade micromanipulator was used to peel off Au electrodes and then transfer them to LED devices.

2.2. Optical Characterization. PL, Raman and EL measurements were conducted using a Horiba LabRAM system equipped with a confocal microscope, a charge-coupled device (CCD) Si detector, and a 532 nm diode-pumped solid-state (DPSS) laser as the excitation source. For temperature-dependent (above 83 K) measurements, the sample was placed into a microscope-compatible chamber with a low-temperature controller (using liquid nitrogen as the coolant). The electrical bias for LED was applied using a Keithley 4200 semiconductor analyzer. The spectral response of the photodetector devices was measured using the conventional amplitude modulation technique with a tungsten-halogen lamp as a white illumination source, a mechanical chopper, an Acton SpectraPro 2300i monochromator, a Stanford SR570 low noise current preamplifier and a Stanford SR830 DSP lock-in amplifier. The two-dimensional photocurrent mapping was performed with a WITec alpha300S scanning microscopy system.

3. RESULTS AND DISCUSSION

Figure 1a and b show the schematic and optical microscope image of the monolayer $MoTe_2$ LED. The single tunneling

DOI: 10.1021/acsami.8b14076
ACS Appl. Mater. Interfaces XXXX, XXX, XXX−XXX

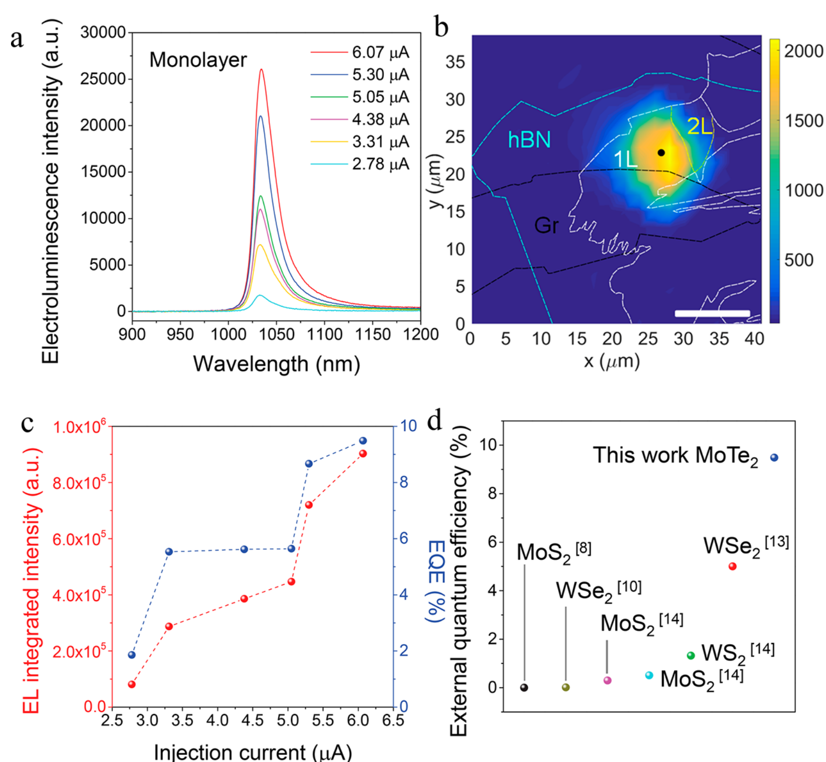

Figure 2. Strong near infrared EL emission at 83 K. (a) EL spectra from monolayer $MoTe_2$ under different injection current and −20 V back gate voltage. The spectra are collected from black dot in b. (b) EL mapping image of the $MoTe_2$ LED device under an injection current of 9.7 μA and −20 V back gate. The blue, white and black dashed line outline hBN, $MoTe_2$, and graphite. Scale bar, 20 μm. (c) EL intensity (left) and EQE (right) of monolayer $MoTe_2$ as a function of the injection current. (d) Quantum efficiency for different monolayer TMD devices.

junction is made of stacked graphite, hexagonal boron nitride (hBN), and monolayer $MoTe_2$ from top to bottom. A monolayer $MoTe_2$ sample identified by a phase shift interferometer (PSI) was first mechanically exfoliated onto a SiO_2/Si (275 nm thermal oxide on n^+-doped silicon) substrate and then the sample was stored in vacuum to avoid any oxidation or contamination (Figure S1). A 6−8 layers hBN identified by PSI was also exfoliated onto the SiO_2/Si substrate for subsequent processes (Figure S2). We used a dry-peel-and-lift van der Waals technique to assemble our devices,[18] and the whole transfer process was solution-free (Supporting Note 1). From bottom to top, $MoTe_2$ monolayer and thin-layer sample with irregular shape (white dashed line in Figure 1b) was mostly covered by a large piece of thin-layer hBN (blue dashed line in Figure 1b), with graphite (black dashed line in Figure 1b) located on top of monolayer-$MoTe_2$/hBN heterostructure serving as one electrode. The top thin-layer hBN serves not only as a tunneling layer to realize device function but also as a capping layer to protect the active $MoTe_2$ layer from contamination to enhance device performance and stability. Figure 1c illustrates the measured Raman spectrum from the monolayer $MoTe_2$/hBN/graphite overlapping area excited with a 532 nm laser. The characteristic phonon response of the A_{1g} at 172.1 cm^{-1} and E_{2g} at 235.9 cm^{-1} is consist with previously report in monolayer $MoTe_2$.[15] The small peak B located at 183 cm^{-1} may be the second order Raman modes of monolayer $MoTe_2$, as observed in other TMDs.[19−21] The Raman peak of hBN was observed at around 1366 cm^{-1}, corresponding to the characteristic peak of E_{2g} phonon mode. This extremely low peak intensity indicates that our hBN flake is very thin, which is consistent with the previous report that the peak intensity becomes progressively weaker as hBN layer number decreases.[22] The characteristic peaks of graphite were also observed in the high frequency region at 1581 cm^{-1} (G band) and 2718 cm^{-1} (2D band).[23] Figure 1d shows typical electroluminescence (EL) and photoluminescence (PL) spectra of our monolayer $MoTe_2$ LED. By applying a negative bias onto top graphite electrode and grounding monolayer $MoTe_2$, electrons and holes would tunnel through the hBN layers into the active $MoTe_2$ monolayer, leading to the$I$−V curve shown in Figure S5. Strong EL from monolayer $MoTe_2$ can be obtained at an even higher temperature (83 K) compared to previous reports,[12,13] as illustrated (red) in Figure 1d. To understand the nature of the EL, the PL spectrum (blue) at 83 K from the same location is also presented. The measured PL spectrum exhibits two clear peaks with central wavelengths at ∼1036 nm (1.197 eV) and ∼1051 nm (1.179 eV) and they are noted as exciton and trion emission from monolayer $MoTe_2$, which matches well with the previous observation.[4] In the PL spectrum, one broad peak located at 1121.6 nm (1.1 eV) can also be observed and is assigned to be the PL emission from n^+-doped silicon (Figure S4). The center peak of the EL spectrum is located at 1034.6 nm (1.198 eV) with 29 meV full-width-at-half-maximum (fwhm). The similar peak positions between the EL and PL spectra and the extremely small fwhm for the EL peak indicate that the EL emission is exciton dominant. Less trion contributions in EL spectrum compared with PL spectrum reflects that the initial doping of our monolayer MoTe2 is slightly n-type after LED device fabrication (Supporting Note 5). The injected electrons and holes would form excitons before the radiative recombination, reflecting the large exciton binding energy at high temperature due to the strong Coulomb interaction in monolayer $MoTe_2$.

DOI: 10.1021/acsami.8b14076
ACS Appl. Mater. Interfaces XXXX, XXX, XXX−XXX

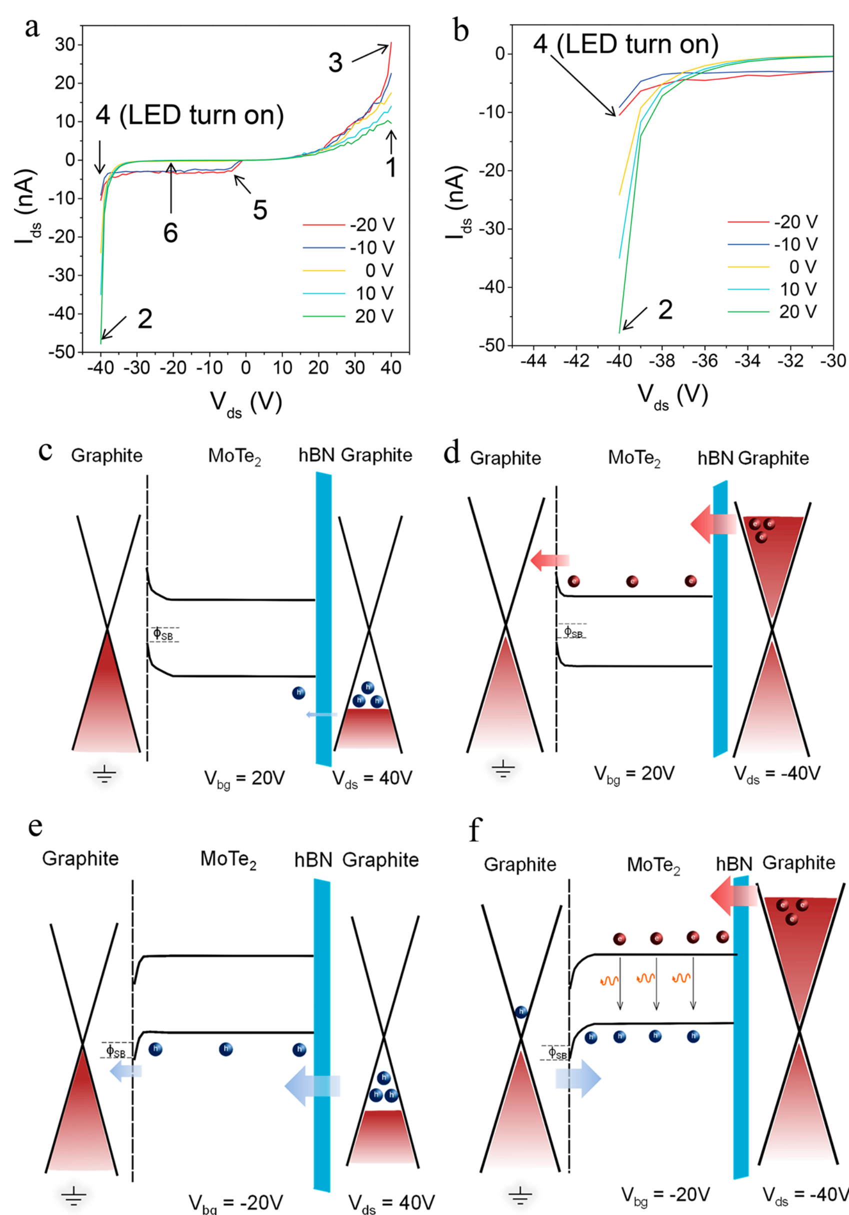

Figure 3. Working principle of the monolayer $MoTe_2$ LED device. (a) $I_{ds} - V_{ds}$ curve for the device under various back-gate voltages at room temperature. States 1 to 6 are marked in different locations. (b) Zoom-in image of the left part of $I_{ds} - V_{ds}$ curve in a. (c) Band diagram of the device operating at state 1 (V_{bg} = 20 V, V_{ds} = 40 V) in a. (d) Band diagram of the device operating in state 2 (V_{bg} = 20 V, V_{ds} = −40 V) in a. (e) Band diagram of the device operating in state 3 (V_{bg} = −20 V, V_{ds} = 40 V) in a. (f) Band diagram of the device operating in state 4 (V_{bg} = −20 V, V_{ds} = −40 V) in a.

Figure 2a shows EL spectra of monolayer $MoTe_2$ LED with increasing injection current. A single EL peak located at 1034.6 nm can be observed from all spectra under different injection currents, indicating that our monolayer $MoTe_2$ remained in high quality after complicated device fabrication process. Figure 2b is a spatial mapping of the EL peak intensity from the $MoTe_2$ LED device at 83 K. Monolayer $MoTe_2$, few-layer hBN, and graphite region is outlined by white, blue, and black dashed line, respectively. The EL mapping shows uniform and strong emission from the entire monolayer $MoTe_2$ region, suggesting that the injected current evenly flows through the monolayer region. The total illuminating area reached around 80 μm^2, which is 10 to 20 times larger than that in typical lateral structure LEDs.[10] With an illuminating area of 80 μm^2, the current density of measured highest EL spectra in Figure 2a is only 75.9 nA/μm^2. The plot of the integrated EL intensity as a function of injection current shows two different slopes with an apparent threshold at 5.05 μA (Figure 2c red curve). The integrated EL intensity increases slowly below the threshold, and it increases dramatically above the threshold. This current threshold may result from the direct tunneling (DT) and Fowler-Nordheim tunneling (FNT) transition (discussed later).[24] Furthermore, the strong EL emission under the small drive current suggests that our device has a very high EQE. Here the EQE is defined as EQE = $eN_{ph}/\eta I$, where e is the electron charge, N_{ph} is the number of photons detected by the detector, η is the system collection efficiency (Figure S3), and I is the current passing through the device active area. Figure 2c shows the EQE as the function of the injection current (blue curve). Similar to the trend of

DOI: 10.1021/acsami.8b14076
ACS Appl. Mater. Interfaces XXXX, XXX, XXX−XXX

integrated EL intensity, the EQE curve also exhibits the doubled-slope feature with the transition at 5.05 μA. We believe that the double-sloped EQE and integrated EL intensity are related to the transition of DT and FNT effect. Apart from the definition of EQE above, the EQE can also be expressed as follows: EQE = $\eta_{radiative}\eta_{injection}\eta_{extraction}$. Here, $\eta_{radiative}$ is the radiative recombination efficiency, $\eta_{Injection}$ is the current injection efficiency and is defined as the fraction of current injected into the QW that recombines radiatively and nonradiatively with respect to the injected and escaped current, and $\eta_{extraction}$ is the extraction efficiency and is defined as the ratio of the generated photon that can be extracted from a device to total photons from a QW.[25] In our experiment, all EL spectra were collected with the same system, and thus $\eta_{extraction}$ was the same for all spectra. The EQE in this case is determined by $\eta_{radiative}$ and $\eta_{injection}$. The radiative recombination efficiency is typically a constant, and this value is mostly determined by material itself. Therefore, the overall EQE is related to current injection efficiency which can be expressed as

$$\eta_{injection} = \frac{I_{QW_total}}{I_{Qw_total} + I_{barrier_total}}$$

where I_{Qw_total} is total recombination current in the $MoTe_2$ layer and $I_{barrier_total}$ is total recombination current in the hBN barrier area. The total injection current (I_{total}) is the sum of both I_{Qw_total} and $I_{barrier_total}$.

Before further discussion, it is necessary to note that our EL measurement was conducted in the small current regime, which is far away from the quantum efficiency saturation or EQE suppression (efficiency droop) regime. Therefore, the escaping current from the QW can be considered to be a small constant. The device operated when electrons were injected into the $MoTe_2$ layer after tunneling through the few-layer hBN barrier. The DT process typically happens at low voltage region, whereas the FNT process dominating at high voltage region (Figure S6). Under small voltage (DT process), electrons in graphite need to tunnel a trapezoidal hBN barrier into the QW (Figure S6a). No matter how high the graphite Femi level rises, the barrier thickness will never change and the current loss in the barrier area ($I_{barrier_total}$) is proportional to I_{total}, which results in a low and uniform current injection efficiency. However, the hBN barrier shape changes from trapezoid to triangle when the tunneling process becomes FNT (Figure S6b) at higher biases. In triangular barrier scenario, the barrier thickness becomes narrower as the graphite Femi level rises, which causes easier tunneling of electrons into the QW and significantly decreased current loss in the barrier area ($I_{barrier_total}$), leading to higher and increasing current injection efficiency, as shown in Figure 2c.

To further demonstrate the high EQE of our device, we have compared the EQE of our monolayer $MoTe_2$ LED with previously reported monolayer TMD-based LEDs, as presented in Figure 2d.[8,10,13,14] For vertical structure LED devices,[13,14] they were both measured in the small injection current regime where the EQE monotonically increases with the injection current and the EQE was recorded at their highest injection current. In our measurement, the highest injection current was much smaller than those in reported devices. The EQE of our device at highest injection current (75.9 nA/μm^2) was measured to be 9.5%, which is nearly twice of what was measured in a monolayer WSe_2 LED with an injection current of 9.4 μA/μm^2.[13] Taking into account the 124 times smaller injection current, the total EQE enhancement reaches a maximum of ~236 times. Such high quantum efficiency in our device arises from two aspects: 1) the delicate device structure, ultra clean interface of devices, dry membrane transfer and photolithography-free electrodes pattern technique; 2) low substrate absorption at the emission wavelength of $MoTe_2$. Considering the vulnerability of the active monolayer $MoTe_2$, our device structure was designed to be an inversion of the common vertical structure.[12] Our PL studies showed that bottom-placed $MoTe_2$ layer successfully avoided surface contamination and sample degradation (Figure S7). Besides, a dry and lithography-free method was used to transfer membranes and to pattern electrodes (Supporting Note 1).[26,27] Therefore, our device was assembled under a totally dry environment and no molecules were introduced from any organic solution, which can be seen in our clear PL spectra without any defect related peaks. Compared to other visible TMD-based LEDs, our monolayer $MoTe_2$ LED has an emission wavelength at ~1035 nm that is very close to the Si bandgap. Silicon has a weak absorption coefficient at 1.1 eV of ~1.5 cm^{-1},[28,29] therefore the emitted light from $MoTe_2$ monolayer is nearly transparent to silicon. By introducing a back-reflecting mirror or other light trapping structure on the back of the substrate, the device EQE can be further improved.

To further understand the tunneling effect of our LED device, we measured its electrical properties. The $I_{ds}-V_{ds}$ curve of the device under different back-gate voltages and corresponding analyzed band diagrams are illustrated in Figure 3. Here we discuss 6 different states labeled in Figure 3a, b. The corresponding band diagrams are presented in Figure 3c–f. The whole device consists of three parts in the band diagram, including Schottky barrier (SB), $MoTe_2$ active layer, and hBN barrier. First, the device is under 20 V back-gate voltage (V_{bg} = 20 V), leading to a relatively large SB between graphite and $MoTe_2$ (State 1 and 2). A positive bias (V_{ds} = 40 V) applied to another graphite electrode lowers the graphite Femi level (E_F) below the valence band (E_V) of gated $MoTe_2$, which induces holes to tunnel through the hBN barrier into $MoTe_2$ layer (State 1, as illustrated in Figure 3c). On the contrary, a negative bias (V_{ds} = −40 V) applied to graphite electrode will raise its E_F above the conduction band (E_C) of gated $MoTe_2$, resulting in electrons tunneling into $MoTe_2$ layer (State 2, as illustrated in Figure 3d). Meanwhile, holes in the other side graphite cannot be injected into $MoTe_2$ monolayer because of the large energy barrier for hole. In the above two scenarios, there is no radiative recombination due to lack of electrons or holes in monolayer $MoTe_2$. Subsequently, state 3 and 4 show that when the device is under −20 V back-gate voltage (V_{bg} = −20 V), the conduction and valence band of $MoTe_2$ bend upward, which narrows the SB width. If the E_F of graphite closed to hBN side is lowered below E_V of the gated $MoTe_2$, holes can also tunnel into $MoTe_2$, similar to the situation in Figure 3c, but with a larger current because of the smaller SB (State 3, as illustrated in Figure 3e). In state 4 (Figure 3f), when our device is under −20 V back-gate voltage (V_{bg} = −20 V) and graphite closed to hBN side is under a large negative bias (V_{ds} = −40 V), electrons in this graphite can tunnel into the $MoTe_2$ monolayer after raising the E_F. In the meantime, holes are also able to tunnel through the SB into $MoTe_2$ monolayer. And then electrons and holes recombine radiatively leading to a great of photon emissions. The state 5 and state 6 illustrate the scenario before our device emitting light, which

DOI: 10.1021/acsami.8b14076
ACS Appl. Mater. Interfaces XXXX, XXX, XXX−XXX

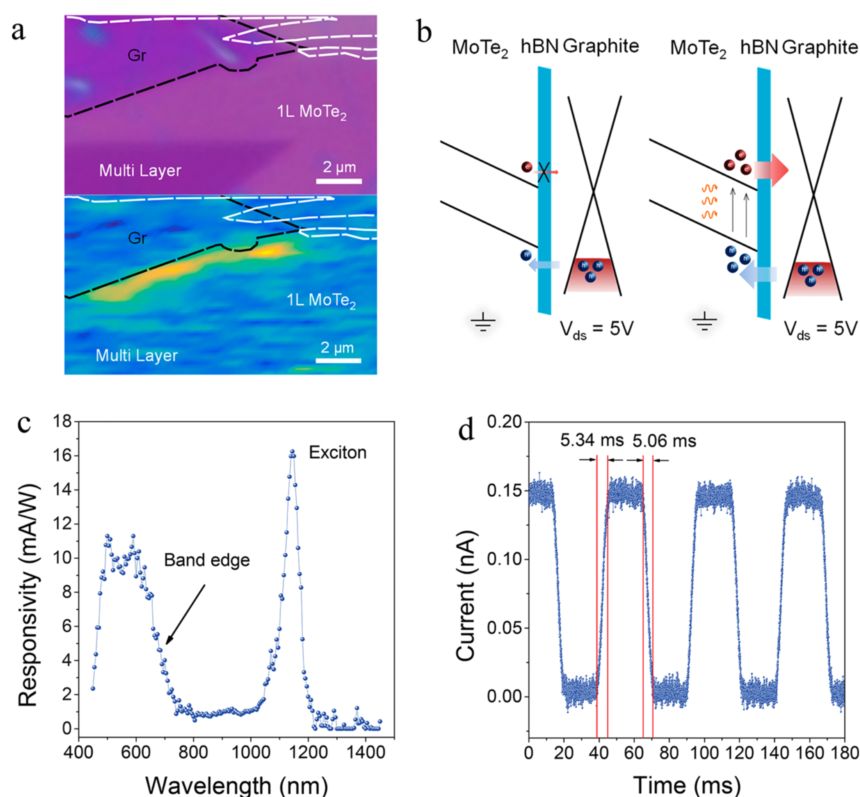

Figure 4. Photoresponse of monolayer $MoTe_2$ photodetector. (a) Top panel: Optical microscope image of the monolayer $MoTe_2$ photodetector. White and black dashed line outline $MoTe_2$ and graphite. Few-layer hBN is located between graphite and $MoTe_2$. Bottom panel: Photocurrent mapping image of the same area. The image is acquired at V_{ds} = 5 V and V_{bg} = 0 V under 532 nm excitation laser (9 nW). (b) Band diagram of the monolayer $MoTe_2$ photodetector. Left and right side show the device working without and with light illumination, respectively. (c) Photoresponsivity as a function of wavelength under 10 nW white light, with V_{ds} = 5 V and V_{bg} = 0 V. (d) Temporal photocurrent of the monolayer $MoTe_2$ photodetector. Incident light: 10 nW white light, V_{ds} = 5 V, V_{bg} = 0 V. The rise time (5.34 ms) is defined as the time of the photocurrent increases to 90% of the ON-state current. The fall time (5.06 ms) is defined as the time for the photocurrent decreases to 10% of the ON-state current.

has been explained in supporting note 3. By modulating the Femi level of the graphite, we can manipulate the injection of electrons and holes in this type of vertical structure device and thereby realize device control.

As the initial doping of the monolayer $MoTe_2$ is quite small,[4] the doping level of $MoTe_2$ could significantly change when it is under different gates.[30] Therefore, it is worth discussing the gate effect on behaviors of the device. First, the source and drain current in Figure 3a, b is compared at a given V_{ds} equals to 40 V. The source and drain current for V_{bg} at −20 V is larger than the V_{bg} at 20 V. When V_{bg} is set at 20 V, the channel type in $MoTe_2$ is n-type and electrons are the majority of charge carriers. In this case, holes injected from tunneling through hBN could not generate large current. However, the channel type in $MoTe_2$ switches to p-type when V_{bg} is set to −20 V. The holes become majority carriers leading to larger current. Conversely, the current for V_{bg} at −20 V is smaller than the V_{bg} at 20 V when the given V_{ds} is at −40 V. In this scenario, electrons are injected through hBN. The channel type changes from p-type to n-type when V_{bg} increasing from −20 to 20 V. Our results are consistent with previous report.[30]

The above electrical and light emitting studies demonstrate excellent optoelectronic performance in our vertical tunneling structure. However, the photodetection property based on $MoTe_2$ material and such tunneling structure are barely reported. Here we have further extended our device into photodetector and conducted some initial characterizations of photo response properties. Figure 4a up-panel shows the optical microscope image of our monolayer $MoTe_2$ photodetector that has the same configuration as our LED device. The monolayer $MoTe_2$ is fully covered by a few-layer hBN flake. The corresponding photocurrent mapping at 5 V bias (V_{ds} = 5 V) with a 532 nm laser excitation (9 nW) is presented in Figure 4a bottom panel, with the graphite and $MoTe_2$ region outlined by black and white dashed line, respectively. The photocurrent mapping clearly indicates that photoresponse comes from the monolayer $MoTe_2$ close to the edge of the graphite. Under 5 V bias, the E_F of graphite is lowered and thus only some of holes can tunnel into the $MoTe_2$ monolayer. This small amount of tunneling holes contributes dark current in this case, as shown in Figure 4b, left panel. By inserting the hBN tunneling layer, the dark current can be highly suppressed. With light illumination, the minority electron population in the conduction band of $MoTe_2$ is significantly enhanced and can tunnel into graphite to generate light current (Figure 4b, right panel). However, photoexcited electrons beyond the carrier diffusion length will recombine radiatively or nonradiatively before arriving the graphite electrode, which causes the photoresponse only showing near the edge of the graphite.

The spectral photoresponsivity of our device is measured and illustrated in Figure 4c. This wavelength-dependent photoresponsivity is largely attributed to light absorption by $MoTe_2$ monolayer. The photoresponsivity is negligible for

DOI: 10.1021/acsami.8b14076
ACS Appl. Mater. Interfaces XXXX, XXX, XXX−XXX

photons with wavelength longer than 1180 nm (energy smaller than 1.05 eV), corresponding to the exciton bandgap of monolayer $MoTe_2$. Apart from $MoTe_2$ exciton photoresponsivity peak, we also observed that the photoresponsivity reached its maximum increase rate at 690 nm, indicating the monolayer $MoTe_2$ band edge, which is consistent with previous report.[4] Remarkably, another strong resonate peak located at 450 nm can also be observed in the spectrum. We attribute this peak to C peak originated from the regions of parallel bands near the Γ point, which rises from the band nesting effect (Supporting Note 2).[4] We also measured the response time of our device, as displayed in Figure 4f. The rise and fall time in our device are 5.34 and 5.06 ms, respectively. Such short response time is attributed to the flat hBN surface above the $MoTe_2$, which minimizes charge transfer at the hBN/$MoTe_2$ interface and again, reflects our ultraclean device fabrication process. Finally, the photodetectivity, one of the most important parameters in the photodetector, indicates the capability of a device to detect weak signal and it can be calculated by using following formula:[17]

$$D = \frac{\mathrm{EQE}(qA)^{1/2}}{h(2I_{\mathrm{dark}})^{1/2}}$$

Where external quantum efficiency EQE = $R(h\upsilon/e)$, q is the elementary charge, h is Planck's constant, $\upsilon = c/\lambda$, c is the speed of light in vacuum, λ is 1145 nm, and I_{dark} is 5×10^{-12} A. The detectivity is calculated to be 2.6×10^9 cm Hz$^{1/2}$ W^{-1}.

4. CONCLUSIONS

In conclusion, we have demonstrated vertical structured high-efficiency monolayer $MoTe_2$ LED for the first time, and it shows extremely high performance with an EQE of ~9.5% at 83 K. The working principle of this vertical tunneling device has been identified by band diagram study under different situations. Such kind of LED presents a huge potential to be future near-infrared on-chip light sources. And their efficiencies can be further improved by creating multiple QWs[13] and delicate tuning of the hBN barrier thickness. Furthermore, this hBN-encapsulated structure can also be extended to photo-detection with strong photoresponsivity and fast response time. Our results open a new route for the investigation of novel infrared optoelectronic devices.

ASSOCIATED CONTENT

Supporting Information

The Supporting Information is available free of charge on the ACS Publications website at DOI: 10.1021/acsami.8b14076.

Figures S1−S10 and Supporting Notes 1−5 (PDF)

AUTHOR INFORMATION

Corresponding Authors

*Email: yuerui.lu@anu.edu.au (Y.L.).
*lan.fu@anu.edu.au (L.F.)

ORCID

Yi Zhu: 0000-0003-2059-3870
Ziyuan Li: 0000-0001-9400-6902
Lan Fu: 0000-0002-9070-8373
Yuerui Lu: 0000-0001-6131-3906

Notes

The authors declare no competing financial interest.

ACKNOWLEDGMENTS

The authors acknowledge the facility support from Prof. Chennupati Jagadish's group at the ANU, Professor Daniel Macdonald from ANU, and ACT node of the Australian National Fabrication Facility (ANFF). The authors acknowledge Financial support from ANU Ph.D. student scholarship, China Scholarship Council, ANU Major Equipment Committee fund (14MEC34), Australian Research Council (ARC) Discovery Early Career Researcher Award (DECRA) (DE140100805) and ARC Discovery Project (DP180103238).

REFERENCES

(1) Mak, K. F.; Lee, C.; Hone, J.; Shan, J.; Heinz, T. F. Atomically Thin MoS_2: A New Direct-Gap Semiconductor. *Phys. Rev. Lett.* **2010**, *105*, 136805.

(2) Zhao, W.; Ribeiro, R. M.; Toh, M.; Carvalho, A.; Kloc, C.; Castro Neto, A. H.; Eda, G. Origin of Indirect Optical Transitions in Few-Layer MoS_2, WS_2, and WSe_2. *Nano Lett.* **2013**, *13*, 5627−34.

(3) Mak, K. F.; He, K.; Lee, C.; Lee, G. H.; Hone, J.; Heinz, T. F.; Shan, J. Tightly Bound Trions in Monolayer MoS_2. *Nat. Mater.* **2013**, *12*, 207−11.

(4) Yang, J.; Lu, T.; Myint, Y. W.; Pei, J.; Macdonald, D.; Zheng, J.-C.; Lu, Y. Robust Excitons and Trions in Monolayer $MoTe_2$. *ACS Nano* **2015**, *9*, 6603−6609.

(5) Zheng, B.; Ma, C.; Li, D.; Lan, J.; Zhang, Z.; Sun, X.; Zheng, W.; Yang, T.; Zhu, C.; Ouyang, G. Band Alignment Engineering in Two-Dimensional Lateral Heterostructures. *J. Am. Chem. Soc.* **2018**, *140*, 11193.

(6) Ye, Y.; Wong, Z. J.; Lu, X.; Ni, X.; Zhu, H.; Chen, X.; Wang, Y.; Zhang, X. Monolayer Excitonic Laser. *Nat. Photonics* **2015**, *9*, 733−737.

(7) Koppens, F. H.; Mueller, T.; Avouris, P.; Ferrari, A. C.; Vitiello, M. S.; Polini, M. Photodetectors Based on Graphene, Other Two-Dimensional Materials and Hybrid Systems. *Nat. Nanotechnol.* **2014**, *9*, 780−93.

(8) Sundaram, R.; Engel, M.; Lombardo, A.; Krupke, R.; Ferrari, A.; Avouris, P.; Steiner, M. Electroluminescence in Single Layer MoS_2. *Nano Lett.* **2013**, *13*, 1416−1421.

(9) Lee, C. H.; Lee, G. H.; van der Zande, A. M.; Chen, W.; Li, Y.; Han, M.; Cui, X.; Arefe, G.; Nuckolls, C.; Heinz, T. F.; Guo, J.; Hone, J.; Kim, P. Atomically Thin P-N Junctions with Van Der Waals Heterointerfaces. *Nat. Nanotechnol.* **2014**, *9*, 676−81.

(10) Ross, J. S.; Klement, P.; Jones, A. M.; Ghimire, N. J.; Yan, J.; Mandrus, D. G.; Taniguchi, T.; Watanabe, K.; Kitamura, K.; Yao, W.; Cobden, D. H.; Xu, X. Electrically Tunable Excitonic Light-Emitting Diodes Based on Monolayer WSe_2 P-N Junctions. *Nat. Nanotechnol.* **2014**, *9*, 268−72.

(11) Liu, C. H.; Clark, G.; Fryett, T.; Wu, S.; Zheng, J.; Hatami, F.; Xu, X.; Majumdar, A. Nanocavity Integrated Van Der Waals Heterostructure Light-Emitting Tunneling Diode. *Nano Lett.* **2017**, *17*, 200−205.

(12) Palacios-Berraquero, C.; Barbone, M.; Kara, D. M.; Chen, X.; Goykhman, I.; Yoon, D.; Ott, A. K.; Beitner, J.; Watanabe, K.; Taniguchi, T.; Ferrari, A. C.; Atature, M. Atomically Thin Quantum Light-Emitting Diodes. *Nat. Commun.* **2016**, *7*, 12978.

(13) Withers, F.; Del Pozo-Zamudio, O.; Schwarz, S.; Dufferwiel, S.; Walker, P. M.; Godde, T.; Rooney, A. P.; Gholinia, A.; Woods, C. R.; Blake, P.; Haigh, S. J.; Watanabe, K.; Taniguchi, T.; Aleiner, I. L.; Geim, A. K.; Fal'ko, V. I.; Tartakovskii, A. I.; Novoselov, K. S. WSe_2 Light-Emitting Tunneling Transistors with Enhanced Brightness at Room Temperature. *Nano Lett.* **2015**, *15*, 8223−8.

(14) Withers, F.; Del Pozo-Zamudio, O.; Mishchenko, A.; Rooney, A. P.; Gholinia, A.; Watanabe, K.; Taniguchi, T.; Haigh, S. J.; Geim, A. K.; Tartakovskii, A. I.; Novoselov, K. S. Light-Emitting Diodes by Band-Structure Engineering in Van Der Waals Heterostructures. *Nat. Mater.* **2015**, *14*, 301−6.

(15) Ruppert, C.; Aslan, O. B.; Heinz, T. F. Optical Properties and Band Gap of Single- and Few-Layer $MoTe_2$ Crystals. *Nano Lett.* **2014**, *14*, 6231−6.
(16) Bie, Y. Q.; Grosso, G.; Heuck, M.; Furchi, M. M.; Cao, Y.; Zheng, J.; Bunandar, D.; Navarro-Moratalla, E.; Zhou, L.; Efetov, D. K.; Taniguchi, T.; Watanabe, K.; Kong, J.; Englund, D.; Jarillo-Herrero, P. A $MoTe_2$-Based Light-Emitting Diode and Photodetector for Silicon Photonic Integrated Circuits. *Nat. Nanotechnol.* **2017**, *12*, 1124−1129.
(17) Yu, W.; Li, S.; Zhang, Y.; Ma, W.; Sun, T.; Yuan, J.; Fu, K.; Bao, Q. Near-Infrared Photodetectors Based on $MoTe_2$/Graphene Heterostructure with High Responsivity and Flexibility. *Small* **2017**, *13*, 1700268.
(18) Pizzocchero, F.; Gammelgaard, L.; Jessen, B. S.; Caridad, J. M.; Wang, L.; Hone, J.; Boggild, P.; Booth, T. J. The Hot Pick-up Technique for Batch Assembly of Van Der Waals Heterostructures. *Nat. Commun.* **2016**, *7*, 11894.
(19) Li, H.; Zhang, Q.; Yap, C. C. R.; Tay, B. K.; Edwin, T. H. T.; Olivier, A.; Baillargeat, D. From Bulk to Monolayer MoS_2: Evolution of Raman Scattering. *Adv. Funct. Mater.* **2012**, *22*, 1385−1390.
(20) Zhao, W.; Ghorannevis, Z.; Amara, K. K.; Pang, J. R.; Toh, M.; Zhang, X.; Kloc, C.; Tan, P. H.; Eda, G. Lattice Dynamics in Mono- and Few-Layer Sheets of WS_2 and WSe_2. *Nanoscale* **2013**, *5*, 9677−9683.
(21) Berkdemir, A.; Gutiérrez, H. R.; Botello-Méndez, A. R.; Perea-López, N.; Elías, A. L.; Chia, C.-I.; Wang, B.; Crespi, V. H.; López-Urías, F.; Charlier, J.-C. Identification of Individual and Few Layers of WS_2 Using Raman Spectroscopy. *Sci. Rep.* **2013**, *3*. DOI: 10.1038/srep01755
(22) Gorbachev, R. V.; Riaz, I.; Nair, R. R.; Jalil, R.; Britnell, L.; Belle, B. D.; Hill, E. W.; Novoselov, K. S.; Watanabe, K.; Taniguchi, T.; Geim, A. K.; Blake, P. Hunting for Monolayer Boron Nitride: Optical and Raman Signatures. *Small* **2011**, *7*, 465−8.
(23) Ferrari, A. C. Raman Spectroscopy of Graphene and Graphite: Disorder, Electron−Phonon Coupling, Doping and Nonadiabatic Effects. *Solid State Commun.* **2007**, *143*, 47−57.
(24) Vu, Q. A.; Lee, J. H.; Nguyen, V. L.; Shin, Y. S.; Lim, S. C.; Lee, K.; Heo, J.; Park, S.; Kim, K.; Lee, Y. H.; Yu, W. J. Tuning Carrier Tunneling in Van Der Waals Heterostructures for Ultrahigh Detectivity. *Nano Lett.* **2017**, *17*, 453−459.
(25) Zhao, H.; Liu, G.; Zhang, J.; Arif, R. A.; Tansu, N. Analysis of Internal Quantum Efficiency and Current Injection Efficiency in Iii-Nitride Light-Emitting Diodes. *J. Disp. Technol.* **2013**, *9*, 212−225.
(26) Pizzocchero, F.; Gammelgaard, L.; Jessen, B. S.; Caridad, J. M.; Wang, L.; Hone, J.; Bøggild, P.; Booth, T. J. The Hot Pick-up Technique for Batch Assembly of Van Der Waals Heterostructures. *Nat. Commun.* **2016**, *7*, 11894.
(27) Zomer, P.; Guimarães, M.; Brant, J.; Tombros, N.; Van Wees, B. Fast Pick up Technique for High Quality Heterostructures of Bilayer Graphene and Hexagonal Boron Nitride. *Appl. Phys. Lett.* **2014**, *105*, 013101.
(28) Green, M. A.; Keevers, M. J. Optical Properties of Intrinsic Silicon at 300 K. *Prog. Photovoltaics* **1995**, *3*, 189−192.
(29) Hull, R. *Properties of Crystalline Silicon*; IET: 1999.
(30) Lin, Y. F.; Xu, Y.; Wang, S. T.; Li, S. L.; Yamamoto, M.; Aparecido-Ferreira, A.; Li, W.; Sun, H.; Nakaharai, S.; Jian, W. B.; et al. Ambipolar $MoTe_2$ Transistors and Their Applications in Logic Circuits. *Adv. Mater.* **2014**, *26*, 3263−3269.

DOI: 10.1021/acsami.8b14076
ACS Appl. Mater. Interfaces XXXX, XXX, XXX−XXX